Supplementary Figures

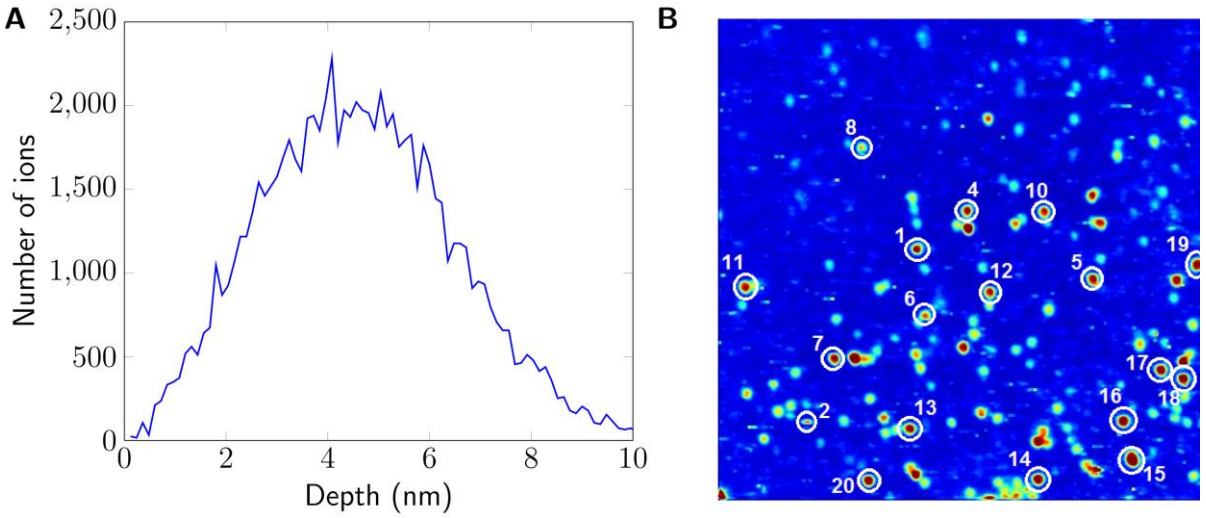

Supplementary Figure 1. Creation of shallow NV centers. (a) SRIM simulation of implantation depth for N^+ ions with an acceleration energy of 2.5 keV. (b) 2.5 keV, N^+ implanted area, showing the measured NVs (NV3 and NV9 are out of the scanning area here).

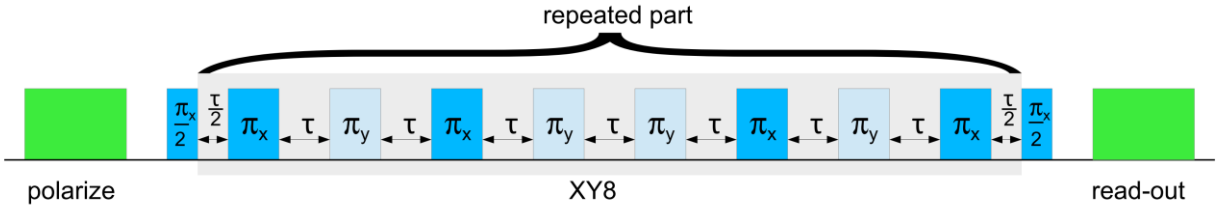

Supplementary Figure 2. Schematic of the XY8-*K* sequence used for measuring nuclear magnetic fields with shallow NV centers. *K* numbers of π pulses are applied to the NV center, where the relative phase of the pulses is adjusted by 0° or 90° depending on whether it is a π_x or π_y pulse.

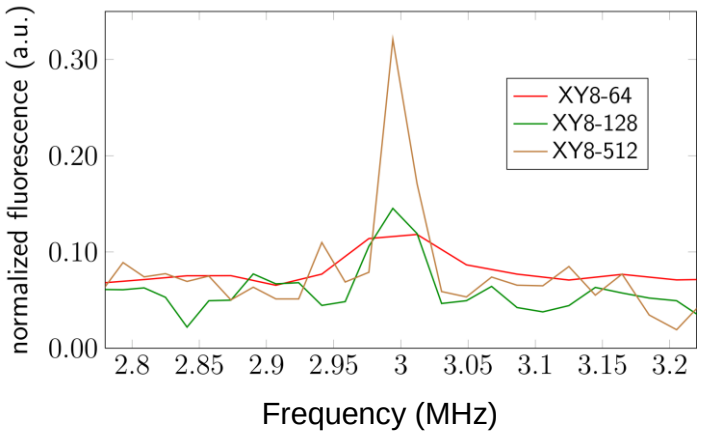

Supplementary Figure 3. The measured NV echo signal after running different XY8-*K* sequences while applying artificial noise at 3 MHz. The full width at half maximum reduces from approximately 40 kHz for XY8-64 to 10 kHz for XY8-512.

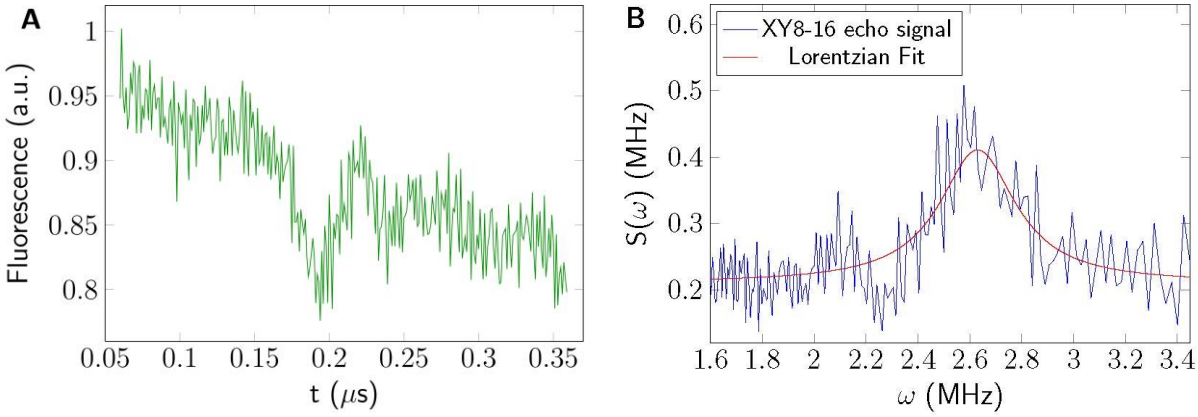

Supplementary Figure 4. Estimation of measured magnetic field from XY8-16 measurement. (a) Echo decay for NV-6 after running the XY8-16 sequence. (b) Power spectral density of the magnetic signal measured with NV-6.

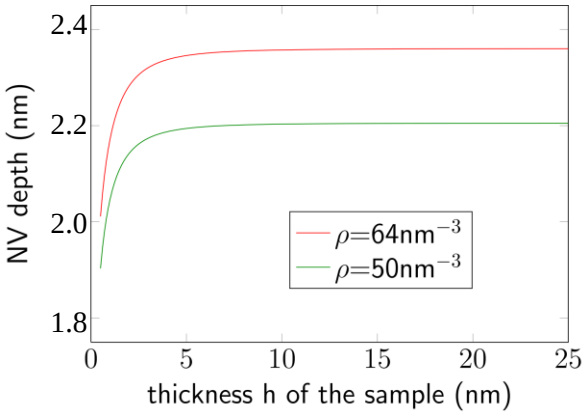

Supplementary Figure 5. Calculated depth of NV-6 as a function of sample thickness for two different simulated proton densities.

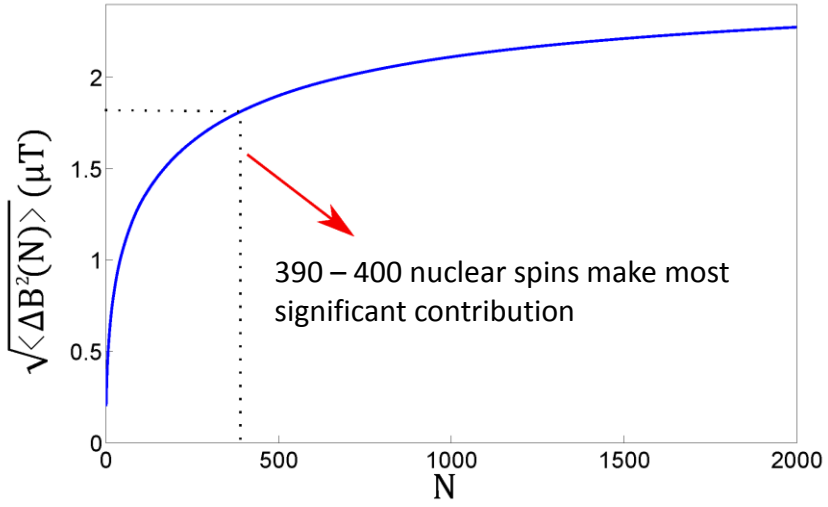

Supplementary Figure 6. Calibration of NV sensing volume. The number of spins that contribute to the measured spin-echo signal is 390-400 ^{1}H nuclei, which corresponds to a volume of 8 nm^{3} in a region above the diamond surface.

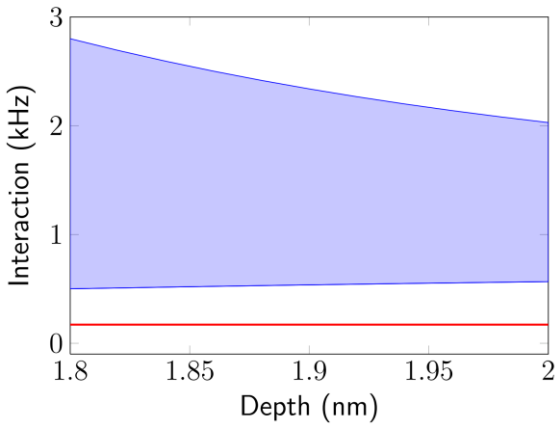

Supplementary Figure 7. The Si-NV spin coupling (blue) compared with the maximum Si-Si direct coupling (red) for different values of NV depth from the configurations of ^{29}Si positions post-selected under the criterion to produce a similar echo decay amplitude as the experimental data.

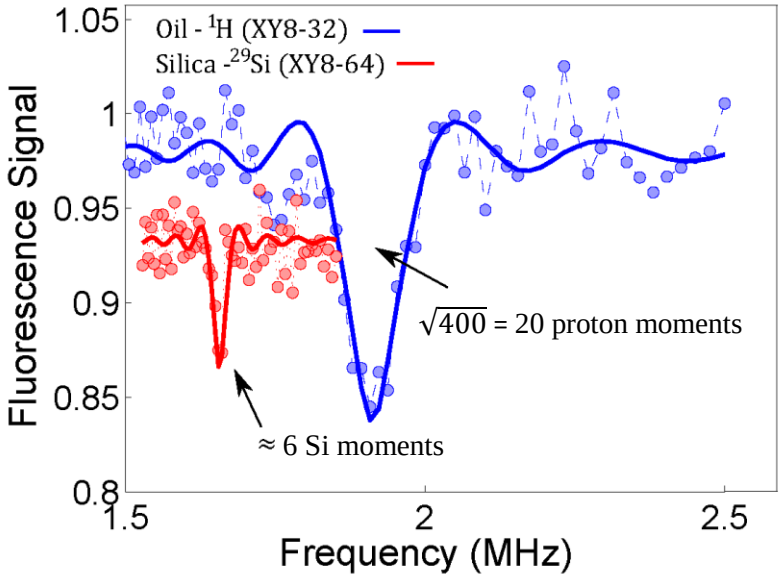

Supplementary Figure 8. Comparison of echo decay from oil and silica samples for NV-6. The echo signal obtained from oil for an XY8-32 measurement at a magnetic field of 0.044 mT is plotted in blue. The echo signal obtained from silica for an XY8-64 measurement at a magnetic field of 0.194 mT is plotted in red. The data has been offset on the vertical scale for clarity.

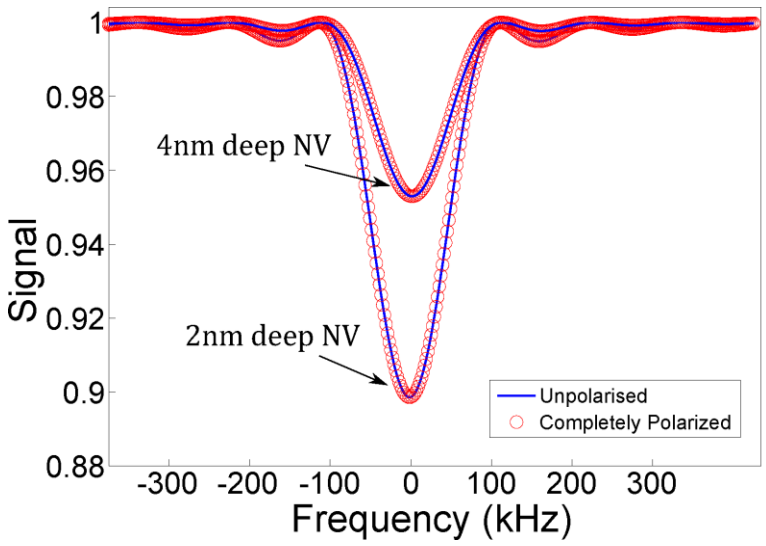

Supplementary Figure 9. Numerical simulations of the signal measured by a single NV center placed at two nanometers and four nanometers distance from 50 completely unpolarised and completely polarized ^{29}Si nuclear spins. The signal is simulated for the XY8-64 pulse sequence.

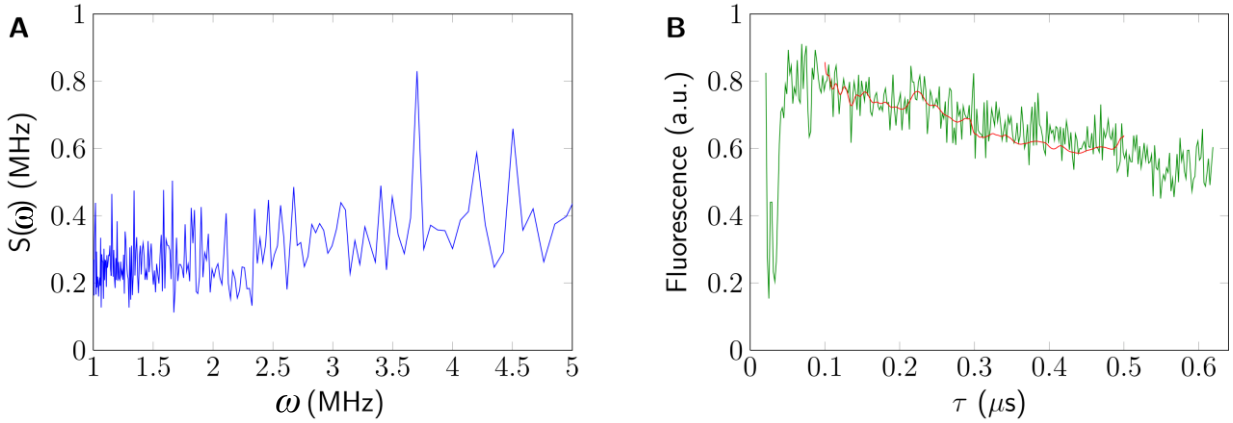

Supplementary Figure 10. Determination of the background noise spectrum from XY8-64 measurement. (a) The estimated power spectra density of the background noise from XY8-64 data. (b) The XY8-64 echo decay reproduced from the estimated background noise spectrum (red) as compared with the experimentally observed echo decay (green).

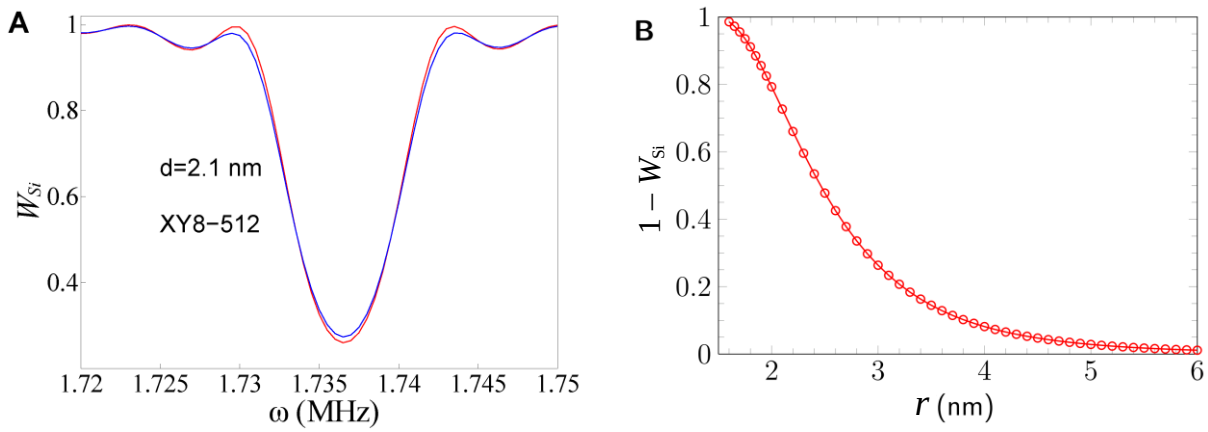

Supplementary Figure 11. NMR signal dynamics as a function of nuclear spin interactions and NV depth. (a) Comparison of the calculated echo decay for a XY8-512 sequence including (blue) and not including (red) Si-Si interactions on a NV center at a depth of 2.1 nm. (b) The echo decay amplitude as a function of NV center depth, *r*.

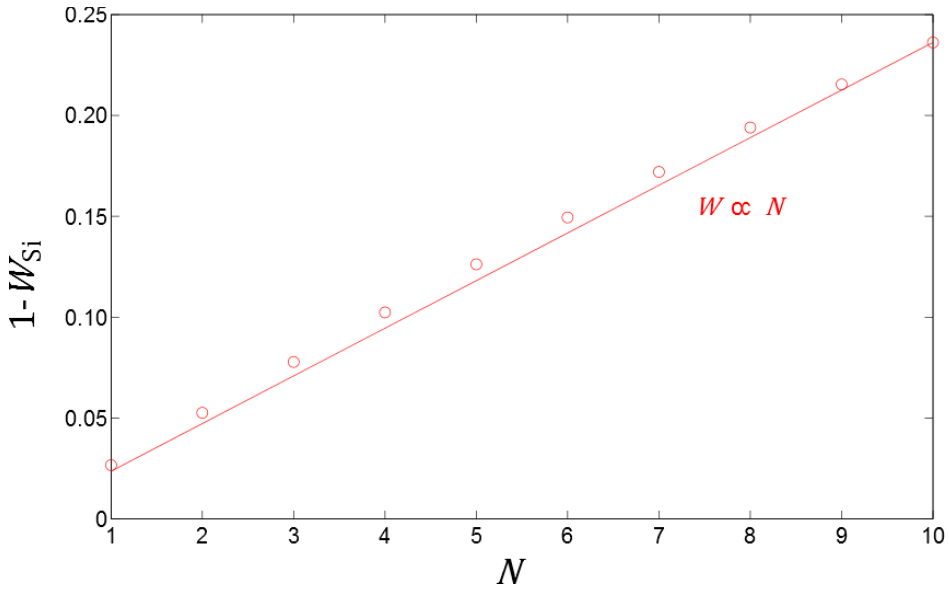

Supplementary Figure 12. The scaling of the XY8-128 signal contrast as a function of the number of interaction nuclear spins, in the strong coupling regime. We assume that the coupling between the NV spin and the nuclear spin is 3 kHz, which is twice as strong as the nuclear-nuclear spin interaction (1.5 kHz). The nuclear Larmor frequency is set as 1 MHz.

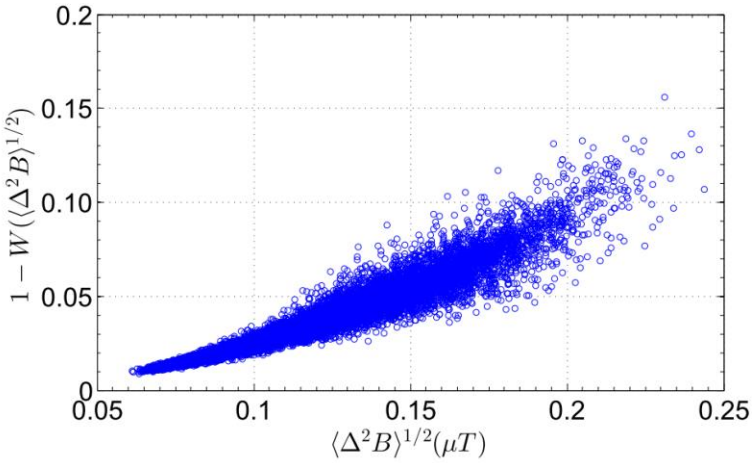

Supplementary Figure 13. The XY8-512 echo decay caused by ^{29}Si as a function of the corresponding magnetic field fluctuation.

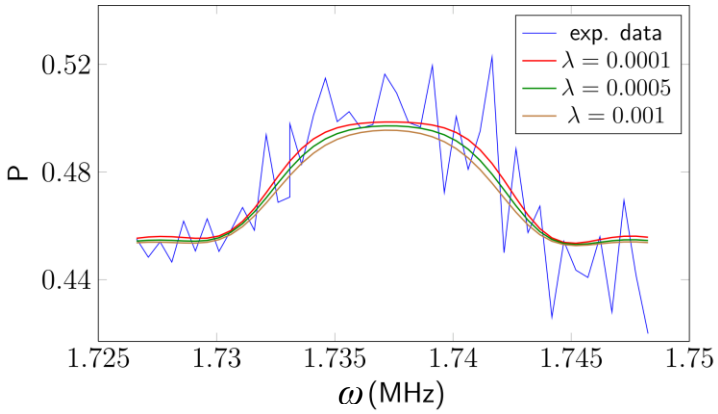

Supplementary Figure 14. The measured signal of experiment with XY8-512 sequence (blue) compared with the fitting data from the basis pursuit denoising (BPDN) analysis with different accuracy control parameter λ.

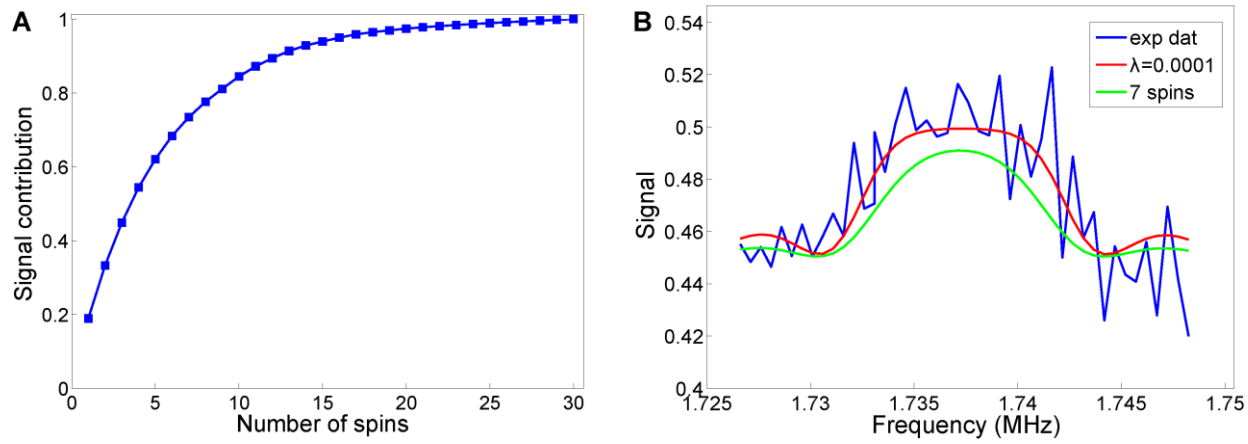

Supplementary Figure 15. Contribution of nuclear spins to NMR signal as recovered from basis pursuit. (a) The overall contribution $p(K_\epsilon)$ of the first K_ϵ nuclei that contribute most significantly the contrast of the echo signal as a function of K_ϵ. (b) The estimated value of K_ϵ as a function of the accuracy control parameter λ used in the basis pursuit denoising (BPDN) analysis.

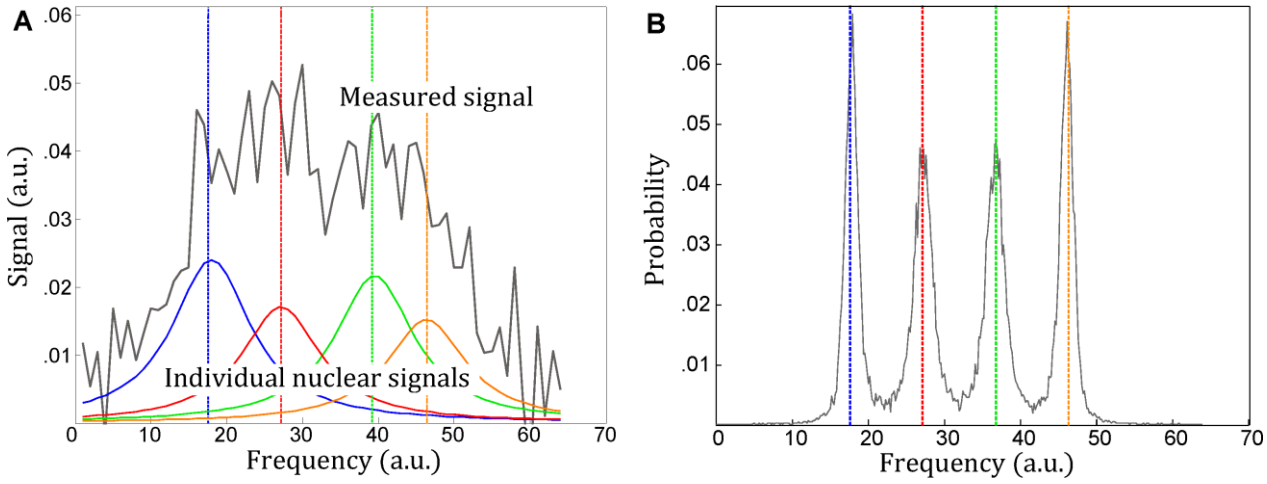

Supplementary Figure 16. An example of the super-resolution properties of basis pursuit. (a) The summed signal from four Lorentzian functions, with Gaussian noise of variance of 0.005 (corresponding to 10% of the signal amplitude) added, is plotted along with the individual functions. Each Lorentzian is an approximation to the signal produced by a single nuclear spin. (b) Histogram of the reconstructed line positions obtained by basis pursuit analysis of 5000 datasets produced in an identical fashion to Supplementary Figure 15a. The obtained line positions are in good agreement to the real line position of the contributing Lorentzian functions, with an error in the obtained line position (at the one standard deviation level), well below the linewidth of each Lorentzian.

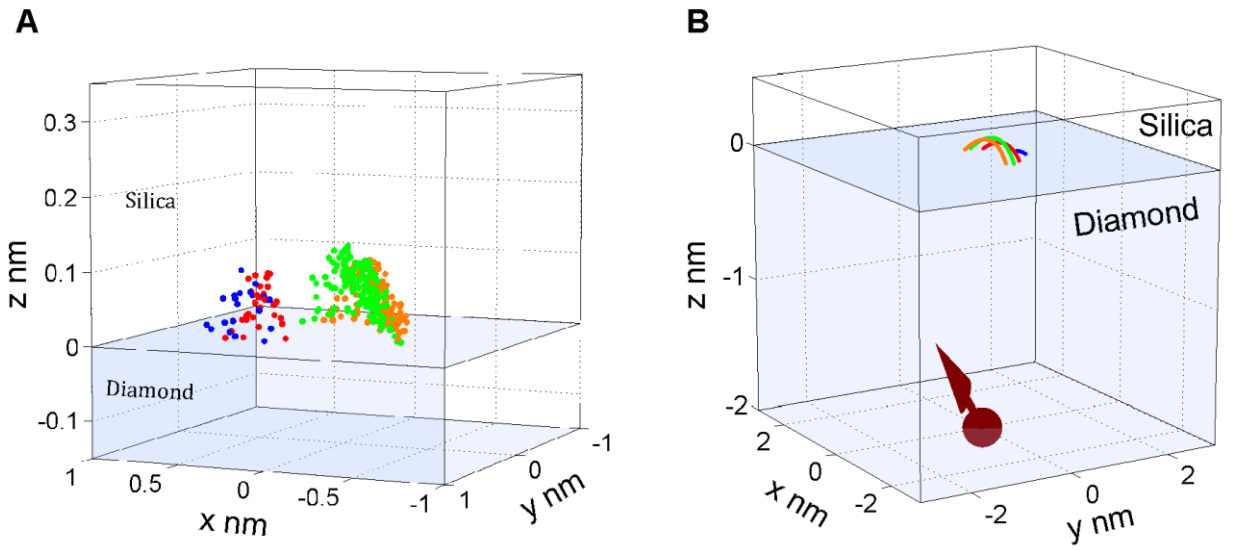

Supplementary Figure 17. Estimated nuclear location uncertainties. (a) The calculated location of each ^{29}Si spin for an uncertainty in the BPDN fit frequency of 0.5 kHz and an uncertainty in amplitude of 0.2. Each fitted value of hyperfine coupling is then compared with a simulation of spins randomly located around the NV center to determine the location. (b) The azimuthal uncertainty in the position of each nuclear spin is shown as an arc above the diamond surface. The circular pattern arises from the circular symmetry of the hyperfine interaction. We obtain a resolution of $(\Delta x_1, \Delta y_1, \Delta z_1) = (0.3\text{nm}, 0.3\text{nm}, 0.03\text{nm})$ for the closest spin and a resolution of $(\Delta x_4, \Delta y_4, \Delta z_4) = (0.4\text{nm}, 0.4\text{nm}, 0.06\text{nm})$ for the furthest spin.

Supplementary Tables

	NV1	**NV6**	**NV7**
$\sqrt{\langle \Delta B^2 \rangle}$ (μT)	2.39	2.58	2.23
depth (nm)	2.4	2.1	2.3

Supplementary Table 1. The estimated depths of NV-1, NV-6, and NV-7 sensors.

Supplementary Note 1. Creation of shallow NV centers

We used chemical vapor deposition grown, 99.999% ^{12}C isotopically purified diamond with an as-grown surface (Element6) and implanted [1] with 3×10^{8} N^{+} ions/cm^{2} with an acceleration voltage of 2.5 keV. For this implantation energy, SRIM [2] simulations reveal an NV center depth between 2 and 7 nm (Supplementary Figure 1a). To identify shallow NV centers we measured the nuclear magnetic signal produced at the Larmor frequency of statistically polarized hydrogen nuclear spins in immersion oil for 20 different NVs (Supplementary Figure 1b).

We used the XY8-*K* dynamical decoupling sequence to measure magnetic fields at the Larmor frequency of ^{1}H. For the initial characterisation, a dense nuclear spin sample of immersion oil was used [3] and the signal remains in the classical regime, therefore we used a classical description of the signal.

Supplementary Note 2. The XY8 decoupling sequence

In the beginning of the sequence the NV center spin is polarized by green laser light (532nm) to the $|0\rangle$ state. A following microwave $\frac{\pi}{2}$ pulse initializes the NV spin into a coherent superposition state $\left(|m_s=0\rangle+|m_s=-1\rangle\right)/\sqrt{2}$. During the dynamical decoupling part (XY8), the NV spin acquires a relative phase $\Delta\varphi$ as $\left(|m_s=0\rangle+e^{i\Delta\varphi}|m_s=-1\rangle\right)/\sqrt{2}$. In the end a second microwave $\frac{\pi}{2}$ pulse converts the phase into a population difference, which can be read-out by another laser pulse.

The XY8-*K* sequence [4] itself consists of equally spaced π pulses along the x and y axes (Supplementary Figure 2):

$$\pi_x - \tau - \pi_y - \tau - \pi_x - \tau - \pi_y - \tau - \pi_y - \tau - \pi_x - \tau - \pi_y - \tau - \pi_x$$

The number *K* is the total number of π pulses for the whole sequence, where the basic XY8 unit is repeated several times. The XY8 sequence suppresses the effect of magnetic field fluctuations except those with frequency $\frac{\omega}{2\pi} = \frac{1}{2\tau}$ (or more precisely $\omega = \frac{\pi}{m\tau}$ with *m* = 1, 3, 5...). By changing the time τ we can tune the detection frequency to the Larmor frequency of the sample spins (^{1}H, ^{29}Si). After repeating the experiment a large number of times, the averaged random phase $\langle \Delta\varphi^2 \rangle$ leads to an observable echo decay as [5]:

$$W(\tau) = \exp\left(-\frac{\langle \Delta\varphi^2 \rangle}{2}\right) = \exp(-\chi(\tau)), \text{ with } \chi(\tau) = \gamma_{\mathrm{NV}}^2 \int_0^\infty \frac{d\omega}{\pi} S(\omega) \frac{F(\omega\tau)}{\omega^2}, \quad \text{(Supplementary Equation 1)}$$

where a factor of 2 comes from the integral extending from $0 \rightarrow \infty$, γ_{NV}^2 is the NV gyromagnetic ratio, $S(\omega)$ is the power spectral density of the magnetic field signal:

$$S(\omega) = \int_{-\infty}^{\infty} \langle B(t)B(0) \rangle e^{i\omega t} dt, \qquad \text{(Supplementary Equation 2)}$$

and $F(\omega\tau)$ is the filter function obtained by application of the XY8-*K* sequence [5]:

$$F(\omega\tau) = 8\sin^4\left(\frac{\omega\tau}{4}\right)\sin^2\left(\frac{\omega K\tau}{2}\right) / \cos^2\left(\frac{\omega\tau}{2}\right). \qquad \text{(Supplementary Equation 3)}$$

The noise power spectrum can be obtained from the measured echo decay by deconvolution of the signal from the filter function. For high orders of the XY8-*K* sequence this filter function can be approximated by a stepwise discrete function:

$$F(\omega\tau) = \begin{cases} 2K^2, & \frac{\omega}{2\pi} \epsilon \left[\frac{1}{2\tau} - \frac{1}{2K\tau}, \frac{1}{2\tau} + \frac{1}{2K\tau}\right]. \\ 0, & \text{otherwise} \end{cases} \quad \text{(Supplementary Equation 4)}$$

The linewidth of the filter function is therefore given by $\Delta\omega \approx \frac{2\pi}{K\tau}$. To show how the linewidth varies with increasing number of π-pulses, different XY8-*K* measurements were performed while applying an artificial noise of 3MHz, which corresponds to the hydrogen Larmor frequency at a magnetic field of around 700 G (Supplementary Figure 3).

With this approximation for the filter function, the echo decay factor can be written as

$$\chi(t = K\tau) = \gamma_{NV}^2 \int_0^\infty \frac{d\omega}{\pi} S(\omega) \frac{F(\omega t)}{\omega^2} = \gamma_{\mathrm{NV}}^2 \frac{4K\tau}{\pi^2} S\left(\omega = \frac{\pi}{\tau}\right), \quad \text{(Supplementary Equation 5)}$$

and therefore we estimate the power spectral density of the magnetic field fluctuation as follows:

$$S\left(\omega = \frac{\pi}{\tau}\right) = \frac{1}{\gamma_{\mathrm{NV}}^2} \frac{\pi^2}{4K\tau} \chi(t = K\tau). \qquad \text{(Supplementary Equation 6)}$$

Supplementary Note 3. Estimation of the NV depth and sensing volume

Measurements were performed at a magnetic field near 616 Gauss, which corresponds to a hydrogen Larmor frequency of 2.6 MHz. About half of the NVs showed a signal from the hydrogen spins and of these, three NVs showed a significantly stronger signal (NV-1, NV-6, NV-7). Supplementary Figure 4a shows the echo-decay signal that we obtained from an XY8-16 sequence for NV-6. The signal is normalized by the Rabi contrast. Supplementary Figure 4b shows the power spectral density calculated from the experimental data in Supplementary Figure 4a, where a peak at the expected frequency (corresponding to t = 0.19 μs) is visible. Measurements at different magnetic fields were performed to ensure that this feature changes frequency in accordance with the gyromagnetic ratio of hydrogen.

The inverse Fourier transformation of the noise spectral density gives the nuclear spin field fluctuation as

$$\langle B(t)B(0)\rangle = \langle \Delta B^2 \rangle = \frac{1}{2\pi}\int_{-\infty}^{\infty} S(\omega)e^{-i\omega t}d\omega. \qquad \text{(Supplementary Equation 7)}$$

The measured magnetic field fluctuation then leads to a depth estimate of between 2.1 and 2.3 nm for NV-6, depending on the density of the oil, see Methods section (Supplementary Figure 5).

The estimated depths for the most shallow NVs are summarized in Supplementary Table 1. To determine the sensing volume, we plot the detected signal of NV-6 as a function of the number of nuclear spins (Supplementary Figure 6), showing that 390-400 nuclei make the most significant contribution to the signal. For a proton density of 50 nm^{-3}, this corresponds to a $(2\ nm)^3$ volume above the diamond surface.

Supplementary Note 4. Comparison of dense proton signal with dilute ^{29}Si signal

Silicon in the SiO_2 sample has a 4.67% abundance of ^{29}Si with a nearest possible distance about 0.3 nm. Based on the information about the depth of NV-7 from the proton data, we calculate the Si-NV coupling strength, as shown in Supplementary Figure 7, which is shown to be much larger than the largest possible Si-Si coupling (about 0.17 kHz for the nearest distance coupling of 0.306nm).

As a first estimation of the number ^{29}Si spins we detect, we compare the echo signal detected from the silica layer with the echo signal detected from the oil. The echo amplitudes are plotted in Supplementary Figure 8, they have been normalized to enable a direct comparison of the signal strength. We note that the signal from ^{29}Si has been detected using an XY8-64 pulse sequence, whereas the ^{1}H signal was obtained with an XY8-32 pulse sequence. The magnetic field was adjusted so that the Larmor frequency of both species was comparable for each measurement. We find that the magnetic signal is a factor of 4 weaker from the silica layer, where we have taken into account the difference in gyromagnetic ratios of the nuclear species, experimental pulse

number and Larmor frequency to make the comparison. This gives an initial estimate that the signal measured for NV-6 arises from interaction with 6 silicon nuclear spins. Calibration for NV-7 gives an interaction with 8 silicon nuclear spins.

Supplementary Note 5. Echo decay from ^{29}Si nuclear spins

Since the interaction between ^{29}Si nuclear spins is much weaker than the interaction between the NV spin and ^{29}Si nuclear spins (see Supplementary Figure 7), we can neglect it. Suppose the NV spin is in the state $|m_s = 0\rangle$ or $|m_s = -1\rangle$, its quantum number will not change during the evolution. The Hamiltonian of the NV spin coupled to a single ^{29}Si nuclear spin at arbitrary location (X, Y, Z) with respect to the NV spin is given by

$$\mathbf{H} = 2\pi\omega_{\mathrm{L}}\mathbf{I}_{\mathrm{Z}} + \frac{\mu_0\gamma_{\mathrm{NV}}\gamma_{\mathrm{Si}}\hbar^2}{4\pi d^3}\mathbf{S}_{\mathrm{Z}}\left(\mathbf{I}_{\mathrm{Z}} - \frac{3Z}{d^2}[\mathbf{I}_{\mathrm{X}}X + \mathbf{I}_{\mathrm{Y}}Y + \mathbf{I}_{\mathrm{Z}}Z]\right) \quad \text{(Supplementary Equation 8)}$$

where μ_0 is the vacuum permeability, $\gamma_{\mathrm{NV}}, \gamma_{\mathrm{Si}}$ are the NV and nuclear gyromagnetic ratios, d is the distance between the NV and nuclear spins, and $\mathbf{S}_i$, $\mathbf{I}_i$ are the NV electron and ^{29}Si nuclear spin operators respectively. The second term of the Hamiltonian can be rewritten as

$$\frac{\mu_0\gamma_{\mathrm{NV}}\gamma_{\mathrm{Si}}\hbar^2}{4\pi d^3}\mathbf{S}_Z\left(\mathbf{I}_{\mathrm{Z}}(1 - 3\cos^2\theta) - \frac{3Z}{d^2}[\mathbf{I}_{\mathrm{X}}X + \mathbf{I}_{\mathrm{Y}}Y]\right) \quad \text{(Supplementary Equation 9)}$$

where θ is the angle between the z-axis and the vector connecting the NV and nuclear spin. The first term gives the parallel component of the hyperfine interaction, and the second term gives the perpendicular component. By summing over N nuclear spins and writing compactly $\mathbf{I}_n^{\perp} \equiv (\mathbf{I}_X, \mathbf{I}_Y)$ we obtain the formula in the main text.

$$\mathbf{H} = \omega_{\mathrm{L}}\sum_n^N \mathbf{I}_n^Z + \mathbf{S}_Z\sum_n^N(\alpha_n\mathbf{I}_n^Z + \beta_n \cdot \mathbf{I}_n^{\perp}) \qquad \text{(Supplementary Equation 10)}$$

The ^{29}Si nuclear spins evolve according to the Hamiltonian conditional on the NV spin quantum number m_s, and the corresponding free evolution during time τ is $\mathbf{U}_{m_s} = exp(-i\tau\mathbf{H})$. It can be shown that the echo decay can be obtained as follows

$$W(\tau) = \mathrm{Re}\, Tr\left(\mathbf{V}_0\mathbf{V}_{-1}^{\dagger}\boldsymbol{\rho}\right), \qquad \text{(Supplementary Equation 11)}$$

where $\mathbf{V}_0 = (\mathbf{U}_0\mathbf{U}_{-1}\mathbf{U}_{-1}\mathbf{U}_0)^4$ and $\mathbf{V}_{-1} = (\mathbf{U}_{-1}\mathbf{U}_0\mathbf{U}_0\mathbf{U}_{-1})^4$, and $\boldsymbol{\rho}$ is the initial state of ^{29}Si nuclear spins. At room temperature ^{29}Si nuclear spins have negligible polarization and thus $=\bigotimes_{\boldsymbol{n}}\left(\frac{\mathbf{1}}{\mathbf{2}}\right)_{\boldsymbol{n}}$. The echo decay arises from the destructive interferences of different evolution path from individual ^{29}Si nuclear spins, even when there is no net ^{29}Si nuclear spin polarization. Considering the simplest case of one single unpolarized ^{29}Si nuclear spin, and assuming that this ^{29}Si nuclear spin is in the state $|I\rangle$, where $|I\rangle = |\uparrow\rangle$ or $|\downarrow\rangle$, the initial state of the combined system of the NV spin and ^{29}Si nuclear spin is $\left(|m_s = 0\rangle|I\rangle + |m_s = -1\rangle|I\rangle\right)/\sqrt{2}$. After the evolution during the XY8-*K* pulse sequence, the state becomes $(|m_s = 0\rangle\mathbf{V}_0|I\rangle + |m_s = -1\rangle\mathbf{V}_{-1}|I\rangle)/\sqrt{2}$, and thus the echo signal is $W_n^{\beta}(\tau) = Re(Tr\langle\beta I|\mathbf{V}_0\mathbf{V}_{-1}^{\dagger}|I\rangle$, where β is the perpendicular component of the hyperfine interaction. For unpolarized ^{29}Si nuclear spins, the echo signal is given by $W_n(\tau) = \frac{1}{2}Re\left(Tr\langle\uparrow|\mathbf{V}_0\mathbf{V}_{-1}^{\dagger}|\downarrow\rangle + Tr\langle\downarrow|\mathbf{V}_0\mathbf{V}_{-1}^{\dagger}|\uparrow\rangle\right)$. With the parameters in our experiments ($\omega_L \gg \alpha_n, \beta_n$), we have verified that the dependence of the signal on the ^{29}Si nuclear spin polarization (along the direction parallel to the magnetic field) is negligible. See Supplementary Figure 9 for results of numerical simulations of the signal measured by an NV center near to completely polarized and completely unpolarised ^{29}Si nuclear spins, the signal is identical for each case.

We separate the contribution from the ^{29}Si and the background noise to the echo decay as

$$W(\tau) = e^{-\chi(k\tau)} \qquad \text{(Supplementary Equation 12)}$$

where

$$\chi(\tau) = \chi_{\mathrm{Si}}(\tau) + \chi_{\mathrm{bg}}(\tau) \qquad \text{(Supplementary Equation 13)}$$

which gives the experimental measured signal

$$C(\tau) = \frac{1}{2}\left[1 + e^{-\chi_{\mathrm{Si}}(\tau)} e^{-\chi_{\mathrm{bg}}(\tau)}\right]. \qquad \text{(Supplementary Equation 14)}$$

The background noise results in the overall decay for all values of τ, while the dip in the signal indicates the contribution from ^{29}Si. From the experiment data, we first extract the power spectra of the background noise by the deconvolution method as explained in the previous section, the result is shown in Supplementary Figure 10.

Supplementary Note 6. Calculation of the magnetic field fluctuation from ^{29}Si

The magnetic field fluctuation acting on the NV center is

$$\langle \Delta B^2 \rangle^{1/2} = \sqrt{\sum_i B_{\mathrm{rms},i}^2} \qquad \text{(Supplementary Equation 15)}$$

and the echo decay is

$$C(\tau) = \frac{1}{2}\left[1 + W\left(\langle \Delta B^2 \rangle^{1/2}\right) W_{\mathrm{bg}}(\tau)\right] = \frac{1}{2}\left[1 + W_{\mathrm{Si}}(\tau) W_{\mathrm{bg}}(\tau)\right]. \qquad \text{(Supplementary Equation 16)}$$

From Supplementary Figure 11a we see that the effect of Si-Si interactions to the total echo amplitude is negligible for a shallow NV center and therefore we did not take those interactions into account in the following analysis. Supplementary Figure 11b shows how the echo decay amplitude decreases strongly with increasing NV center depth. The form of the decay amplitude

is in close agreement to an r^{-3} curve which is expected for an NV center strongly coupled to individual nuclei, rather than $r^{-3/2}$ for an NV center interacting with a bath of spins in the half-plane.

In addition we find that for short interaction times ($\tau < {}^{1}/_{\beta_n}$) the signal contrast, $1 - W_{\mathrm{Si}}$ scales linearly with the number of interacting spins (Supplementary Figure 12). As the decay amplitude also depends on the precise location of each nuclear spin due to the spatial anisotropy of the hyperfine interaction (see Supplementary Figure 13), we assume that each nuclear spin has the same coupling to the NV center. In Supplementary Figure 12, we plot the signal contrast obtained from the full Hamiltonian of the NV spin and the nuclear spins, including the interaction between nuclear spins, which are assumed to be weaker than the interaction between the NV spin and the nuclear spins. The overall signal scales linearly with the number of nuclear spins, i.e. it is the sum of the signal from individual nuclear spins.

Supplementary Note 7. Analysis of the echo decay by basis pursuit

The experimental signal obtained after XY8-512 is plotted in Supplementary Figure 14 and also in Figure 3 of the main text. Note that the measured quantity is the population of the complementary state, denoted as $P(\tau)$. The echo decay thus is $C(\tau) = 1 - P(\tau)$. The obtained signal in Supplementary Figure 14 is inhomogenously broadened compared to the linewidth of the filter-function (see Supplementary Equation 4 and Supplementary Figure 3) due to the NV magnetic gradient. For the data analysis we employ the method of basis pursuit denoising (see Methods). We show in Supplementary Figure 14, the effect of varying the parameter λ on the fit to experimental data. The fit from BPDN agrees well with the data and is robust when varying λ.

In the strong coupling regime, there is no longer a one-to-one correspondence between the magnetic field from a single nuclear spin and the echo signal. We show this graphically in Supplementary Figure 13, highlighting that as the measurable field increases (by bringing the ^{29}Si closer to the NV), the echo amplitude diverges.

To quantify the contribution of individual spins to the overall echo decay we sort the contribution $\chi_{\mathrm{Si}}^{(j)}$ of individual ^{29}Si in descending order, and define the combined contribution by the first K_ϵ ^{29}Si to the contrast of the echo signal as

$$p(K_\epsilon) = S_a([1, K_\epsilon])/S_a([1, J]), \qquad \text{(Supplementary Equation 17)}$$

where $S_a([1, K_\epsilon])$ represents the integral area of the signal contributed by the nuclear spins in the set of $[1, K_\epsilon]$ and $S_a([1, J])$is the integral area of the total signal contributed by all nuclear spins.

The results are plotted in Supplementary Figure 15a, from which we estimate that 6 – 7 ^{29}Si make the most significant contribution (above 70%) to the echo signal (i.e. $p(K_\epsilon) \geq 70\%$), The estimation for the minimum number of ^{29}Si, which may result in the observed signal, is quite robust when varying the parameter λ in BPDN as long as the fitting is above a certain confidence level. In Supplementary Figure 15b we plot to contribution of seven nuclei to the signal, showing close resemblance to the total signal.

Supplementary Note 8. Recovery of nuclear positions by basis pursuit

The stability of basis pursuit in the presence of noise has been demonstrated mathematically in Ref. [6]. Here we provide an illustrative example of the super-resolution properties of basis pursuit denoising, i.e. that frequency components may be recovered with a higher resolution than

given by the measurement linewidth. Indeed, detailed information on the location of the spins contributing to the signal shown in Figure 3a may be obtained, despite the noisy and rather featureless lineshape.

In Supplementary Figure 16a, we plot the combined signal produced by four Lorentzian functions with comparable noise and resolution to the dataset of Figure 3a. The resulting signal appears featureless and with a linewidth much greater than each of the component signals. In Supplementary Figure 16b, we plot a histogram of the determined line centers that were obtained from basis pursuit analysis of 5000 realisations of the same Lorentzian functions (with independent, randomly generated noise for each dataset). The results of the basis pursuit analysis show that, in general the line position can be found very accurately. The standard deviation of the obtained line position is well below the individual Lorentzian linewidth and the mean value is centered on each line position.

Supplementary Note 9. Uncertainty in nuclear locations

To analyze the uncertainty in the nuclear locations, we note that the determined location of each nuclear spin can vary due to both the circular degree of symmetry around the NV axis (which means the azimuthal angle of the nuclear spin with respect to the NV axis is unknown), and also due to uncertainty in the BPDN fit. We first estimate the uncertainty in the fitted location due to the noise in the raw data. We take the uncertainty in the fitted amplitude from BPDN to be comparable to the shot noise of the data, and the uncertainty in the fitted frequency to be 0.5 kHz (comparable to the frequency spacing of the basis functions). From these uncertainties we can plot the recovered positions of the nuclear spins (see Supplementary Figure 17a). We can see that the uncertainty in the location of the weakest coupled ^{29}Si spin (colored orange) is much greater

that the uncertainty in the location of the strongest coupled spin (colored red). This is because for spins that are further from the NV center, small changes in coupling strength correspond to larger changes in distance to the NV. Taking the standard deviation of the location in each direction $(\Delta x, \Delta y, \Delta z)$ we find that for the closest spin $(\Delta x_1, \Delta z_1) = (0.1\text{nm}, 0.02\text{nm})$ and for the fourth spin we obtain an uncertainty in the position of $(\Delta x_4, \Delta z_4) = (0.15\text{nm}, 0.1\text{nm})$.

The circular symmetry of the hyperfine pattern also means that even if the distance and polar angle of individual spins with respect to the NV center is known perfectly, the azimuthal angle is completely unknown. However as the detected spins lie very close to the diamond surface, the circle of symmetry (around the NV axis) intersects with the diamond after only several tens of milliradians. As a result the uncertainty in the both the height of each nuclear spin and its location along this arc also has a very small standard deviation. In Supplementary Figure 17b the possible position of each nuclear spin is shown as an arc above the diamond surface. The x and y axes have been rotated so that the uncertainty in both directions is equal. For the closest spin, we find that $(\Delta x_1, \Delta y_1, \Delta z_1) = (0.1\text{nm}, 0.1\text{nm}, 0.05\text{nm})$, and for the furthest spin we obtain $(\Delta x_4, \Delta y_4, \Delta z_4) = (0.5\text{nm}, 0.5\text{nm}, 0.08\text{nm})$.

Supplementary Note 10. Rotating the magnetic field to determine nuclear locations

In the low magnetic field regime (<100 Gauss) and the high magnetic field regime (>>1 kGauss), the NV spin polarisation and readout is largely unaffected by small misalignments of the magnetic field, and then the B field angle may be changed to locate each nuclear spin. We operated in the intermediate range, where small misalignment of the magnetic field with respect to the NV axis strongly influences the NV spin polarisation and readout. A further complicating factor is that the host ^{15}N nuclear spin of the NV center becomes rapidly entangled with the NV

electron spin as the angle of the magnetic field is changed, producing a frequency artefact in the signal which needs to be carefully removed.

Supplementary References

1 J. Meijer, B. Burchard, M. Domhan, C. Wittmann, T. Gaebel, I. Popa, F. Jelezko & J. Wrachtrup. "Generation of single colour centers by focused nitrogen implantation". *Applied Physics Letters* **87**, 261909 (2005).

2 J.F. Ziegler, M.D. Ziegler & J.P. Biersack. "SRIM – The stopping and range of ions in matter". *Nuclear Instruments and Methods in Physics Research Section B* **268**, 1818 (2010).

3 T. Staudacher, F. Shi, S. Pezzagna, J. Meijer, J. Du, C. A. Meriles, F. Reinhard and J. Wrachtrup. "Nuclear Magnetic Resonance Spectroscopy on a (5-Nanometer)^3 Sample Volume". *Science* **339**, 561-563 (2013).

4 T. Gullion, D. B. Baker, M. S. Conradi. "New, compensated Carr-Purcell sequences". *Journal of Magnetic Resonance* **89**, 479-484, (1990).

5 L. Cywinski, R.M. Lutchyn, C.P. Nave & S. Das Sarma. "How to enhance dephasing time in superconducting qubits". *Physical Review B* **77**, 174509 (2008).

6 D.L. Donoho & M. Elad. "On the stability of the basis pursuit in the presence of noise". *Signal Processing* **86**, 511-532 (2006).